Atomic-scale control of magnetic anisotropy via novel spin–orbit coupling effect in $La_{2/3}Sr_{1/3}MnO_3/SrIrO_3$ superlattices

Di Yi[a,1,2], Jian Liu[b,c,d,1,2], Shang-Lin Hsu[a,e], Lipeng Zhang[f], Yongseong Choi[g], Jong-Woo Kim[g], Zuhuang Chen[a], James D. Clarkson[a], Claudy R. Serrao[a], Elke Arenholz[h], Philip J. Ryan[g], Haixuan Xu[f], Robert J. Birgeneau[a,c,d], and Ramamoorthy Ramesh[a,c,d]

[a]Department of Materials Science and Engineering, University of California, Berkeley, CA 94720; [b]Department of Physics and Astronomy, University of Tennessee, Knoxville, TN 37996; [c]Department of Physics, University of California, Berkeley, CA 94720; [d]Materials Science Division, Lawrence Berkeley National Laboratory, Berkeley, CA 94720; [e]National Center for Electron Microscopy, Lawrence Berkeley National Laboratory, Berkeley, CA 94720; [f]Department of Materials Science and Engineering, University of Tennessee, Knoxville, TN 37996; [g]Advanced Photon Source, Argonne National Laboratory, Argonne, IL 60439; and [h]Advanced Light Source, Lawrence Berkeley National Laboratory, Berkeley, CA 94720, USA

Edited by Zachary Fisk, University of California, Irvine, CA, and approved April 15, 2016 (received for review December 15, 2015)

Magnetic anisotropy (MA) is one of the most important material properties for modern spintronic devices. Conventional manipulation of the intrinsic MA, i.e., magnetocrystalline anisotropy (MCA), typically depends upon crystal symmetry. Extrinsic control over the MA is usually achieved by introducing shape anisotropy or exchange bias from another magnetically ordered material. Here we demonstrate a pathway to manipulate MA of 3*d* transition-metal oxides (TMOs) by digitally inserting nonmagnetic 5*d* TMOs with pronounced spin–orbit coupling (SOC). High-quality superlattices comprising ferromagnetic $La_{2/3}Sr_{1/3}MnO_3$ (LSMO) and paramagnetic $SrIrO_3$ (SIO) are synthesized with the precise control of thickness at the atomic scale. Magnetic easy-axis reorientation is observed by controlling the dimensionality of SIO, mediated through the emergence of a novel spin–orbit state within the nominally paramagnetic SIO.

complex oxides | interfacial physics | magnetic anisotropy | emergent magnetism | strong spin–orbit coupling

Magnetic anisotropy (MA) is one of the fundamental properties of magnetic materials. The widespread scientific interest in MA originates from its decisive role in determining a rich spectrum of physical responses, such as the Kondo effect (1), the magnetocaloric effect (2), magnetic skyrmions (3), etc. From a technological viewpoint, it is an important and promising approach to control MA by external stimuli, such as electric field (4). In general, there are two approaches to design MA of a ferromagnet. In the first approach one manipulates the intrinsic magnetocrystalline anisotropy (MCA), deriving from the local crystal symmetry and spin–orbit coupling (SOC) of the magnetic ion (5–7). Alternatively, one can tune the MA through extrinsic contributions to the anisotropy such as shape (8) or exchange coupling to a strong antiferromagnet (9).

One focus of magnetism research is 3*d* transition-metal oxides (TMOs), a class of materials that exhibit various functionalities including ferromagnetism due to the strong electron–electron correlation. However, SOC is usually weak or negligible in 3*d* TMOs. On the other hand, the pronounced SOC of heavy elements has drawn attention in recent years due to the emergence of new topological states of matter (10–12) and spintronics (13, 14). In contrast to 3*d* TMOs, the correlation strength is often too small in 5*d* TMOs to host magnetism. Therefore, it is an interesting approach to design systems that combine the merits of these two fundamental interactions. A similar ideal has been studied in metal multilayers (15, 16). However, it still remains an important challenge to explore the ideal in complex oxides, where a variety of emergent phenomena have been discovered due to the power of atomic-scale confinement and interfacial coupling (17–21).

Here we present an approach toward accomplishing this goal by atomic-scale synthesis. By fabricating high-quality superlattices comprising 3*d* and 5*d* TMOs, we address two open questions: the effect of SOC on the functionality of 3*d* TMOs and the possible emergent magnetic state of 5*d* TMOs. So far this approach has been limited and overlooked. To the best of our knowledge, $SrTiO_3/SrIrO_3$ is the only 3*d*/5*d* superlattice that has been experimentally studied (22) that reveals the effect of dimensional confinement. However, the 3*d* state is rather inactive in that system. Here we study a model system comprising ferromagnetic $La_{2/3}Sr_{1/3}MnO_3$ (LSMO) and paramagnetic $SrIrO_3$ (SIO). We have discovered that the magnetic easy axis of LSMO rotates between two crystallographic directions, i.e., ⟨100⟩ and ⟨110⟩ (pseudocubic) by digitally reducing the SIO thickness down to one monolayer. Remarkably, the reorientation of MA is accompanied by the emergence of a large, spontaneous, orbital-dominated magnetic moment of the 5*d* electrons, revealing a heretofore-unreported SOC state.

Results and Discussion

The colossal magnetoresistive system LSMO is a 3*d* ferromagnet with a high Curie temperature (23). Due to the potential for applications in all-oxide spintronics, the MA of LSMO thin films has been investigated extensively. Previous studies have

Significance

Interfaces of transition-metal oxides (TMOs) offer a fertile platform to uncover emergent states, which has been extensively explored in 3*d* TMOs with strong electron correlations. Recently research on 5*d* TMOs with pronounced spin–orbit coupling (SOC) is flourishing due to the emergence of new topological states and potential application in spintronics. Interfaces between 3*d* and 5*d* TMOs provide a unique test bed to combine the merits of these two fundamental interactions. However, so far research is limited. Here we present results on one model system comprising the ferromagnet $La_{2/3}Sr_{1/3}MnO_3$ and the strong SOC paramagnet $SrIrO_3$. We observe a manipulation of the magnetic anisotropy by tuning the $SrIrO_3$ dimensionality, which is accompanied by a novel SOC state in $SrIrO_3$.

Author contributions: D.Y., J.L., R.J.B., and R.R. designed research; D.Y. and J.L. performed research; S.-L.H., L.Z., Y.C., J.-W.K., Z.C., J.D.C., C.R.S., E.A., P.J.R., and H.X. contributed new reagents/analytic tools; D.Y., J.L., S.-L.H., L.Z., Y.C., J.-W.K., E.A., P.J.R., H.X., R.J.B., and R.R. analyzed data; and D.Y., J.L., P.J.R., R.J.B., and R.R. wrote the paper.

The authors declare no conflict of interest.

This article is a PNAS Direct Submission.

Freely available online through the PNAS open access option.

[1]D.Y. and J.L. contributed equally to this work.

[2]To whom correspondence may be addressed. Email: yid@berkeley.edu or jianliu@utk.edu.

This article contains supporting information online at www.pnas.org/lookup/suppl/doi:10.1073/pnas.1524689113/-/DCSupplemental.

established the magnetic easy axis of an epitaxial LSMO thin film on (001)-oriented $SrTiO_3$ (STO) substrate to be in-plane along the crystallographic ⟨110⟩ (7, 24) as a consequence of the strain superimposed on the intrinsic rhombohedral symmetry. SIO is an end member of the Ruddlesden–Popper (RP) series $Sr_{n+1}Ir_nO_{3n+1}$ (25). It has been identified to be a SOC paramagnet without any signature of long-range magnetic ordering (26, 27), likely due to the topological nature of its metallicity (28, 29). Owing to the structural compatibility, it has been theoretically proposed as a key building block for stabilizing topological phases at interfaces and in superlattices (12, 30). To investigate the impact of artificial confinement and interfacial coupling, we intentionally insert *m* unit cells (uc) of SIO every 3 uc of LSMO, with *m* being varied from 10 to 1 to scale down the SIO layer from 4 to 0.4 nm (labeled as SL3*m*). All of the superlattices are deposited on STO (001) substrates. The precise control of thickness is achieved by monitoring the intensity oscillations of the reflection high-energy electron diffraction (RHEED) pattern during the growth (Fig. S1), revealing the layer-by-layer growth mode of both LSMO and SIO. This growth mode is critical for synthesizing high-quality superstructures. Details of the synthesis protocols used in our study are provided in *Materials and Methods*.

The high quality of the superlattices characterized by several techniques demonstrates the precise control of thickness at the atomic scale. Fig. 1*A* shows a scanning transmission electron microscopy (STEM) image of a superlattice with differing periodicities in repeated patterns. The sharp Z contrast of B-site species across the interface, supplemented by the line profile of the electron energy loss spectroscopy (EELS) of A-site La atoms (Fig. S2), indicates minimal interdiffusion at the interface. Fig. 1*B* shows the high-resolution θ-2θ X-ray diffraction (XRD) of the SL31 and SL35. The satellite peaks corresponding to the superlattice structure and the finite-size oscillations arising from the thickness are pronounced, suggesting the high degree of interface abruptness and agreement with the intended periodicity. Fig. 1*C* shows the reciprocal spacing mapping (RSM) of sample SL35, revealing that the superlattice is coherently strained by the STO substrate. Further structural characterization data are shown in Fig. S1.

The temperature dependence of the magnetization of the superlattices (Fig. S4) is similar to that of pure LSMO thin film (albeit with a decrease of T_c as *m* increases), indicating that the overall magnetization is dominated by the ferromagnetic LSMO component. To study the MA, magnetization loops are measured along different crystallographic axes of SL3*m* (*Materials and Methods*). First, the magnetic easy axis is revealed to be in the film plane by comparing the in-plane and out-of-plane magnetic loops (Fig. S4), consistent with our expectations (due to the strain effect and shape anisotropy). Additionally, magnetization loops along symmetry-equivalent in-plane directions, e.g., [100] and [010] (Fig. 2*B*), demonstrate that the MA is biaxial (fourfold rotational symmetry with $\pi/2$ periodicity), which is indicative of MCA, and thus rules out the influence of shape anisotropy (8).

The impact of SIO is demonstrated by the systematic influence of the SIO layer thickness on the MA (Fig. 2*A*), which is represented by the normalized difference between the remnant magnetization along ⟨100⟩ and ⟨110⟩ directions. The positive sign corresponds to the ⟨100⟩ easy axis whereas the negative sign indicates a $\pi/4$ shift to ⟨110⟩. As can be seen, the superlattices with long periodicity ($m > 5$, i.e., 2 nm) exhibit ⟨110⟩ easy axis, identical to that of pure LSMO thin film (purple dot, Fig. 2*A*). Intriguingly, as *m* reduces ($m < 5$), a reorientation of the easy axis to ⟨100⟩ is observed. The magnitude of the normalized difference systematically increases as *m* decreases, revealing a tunability of ~40% (theoretical limit ~58% of the biaxial MA; magnetic moments aligning along one direction have a $\pi/4$ projection on the other direction). We also carried out anisotropic magnetoresistance (AMR) measurements to validate the observed MA. The longitudinal resistance is measured along the ⟨100⟩ direction and the magnetic field is rotated in-plane with respect to the current direction (*Materials and Methods*). Fig. 2*C* shows the polar plots of AMR of SL33 and SL310. The fourfold rotation of AMR reflects the same symmetry of the MCA. The $\pi/4$ phase shift of AMR between SL33 and SL310 is coincident with the MA evolution shown in Fig. 2*A*. Further analysis of the AMR of SL3m is shown in Fig. S5 and confirms the change of MA as the SIO thickness reduces. The temperature dependence of the MA (⟨100⟩ easy axis) is acquired by measuring

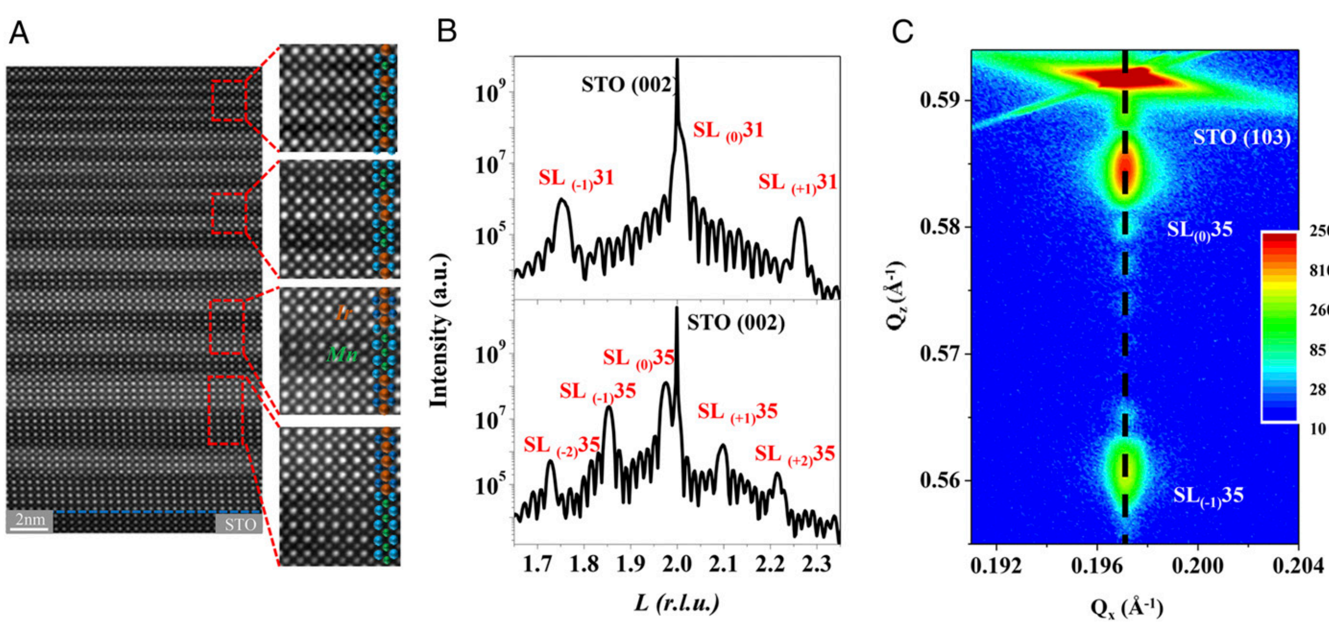

Fig. 1. Structural characterization of the LSMO/SIO superlattice. (*A*) High-angle annular dark-field (HAADF) STEM images of LSMO/SIO superlattice with designed periodicities in one sample. The four high-magnification images correspond to the regions of $(LSMO)_1/(SIO)_1$, $(LSMO)_2/(SIO)_2$, $(LSMO)_3/(SIO)_3$, and $(LSMO)_5/(SIO)_5$ from top to bottom (the number refers to the thickness in uc). The atoms are marked by different colors: Ir (brightest contrast) in orange, Mn (darkest contrast) in green, and A-site atoms in blue. (*B*) θ-2θ X-ray diffractograms of an SL31 (*Top*) and an SL35 (*Bottom*) superlattice. Both the superlattice peaks and the thickness fringes reveal the high degree of interface abruptness. (*C*) X-ray reciprocal spacing mapping of an SL35 superlattice around (103) peak, confirming coherent growth of the superlattice.

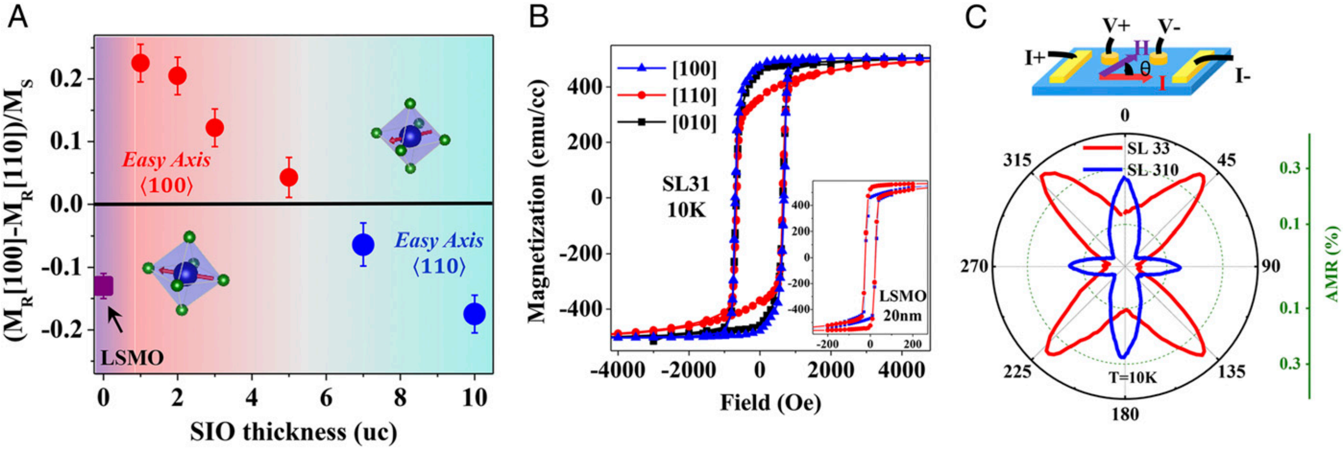

Fig. 2. Magnetic and transport characterization of the LSMO/SIO superlattice. (*A*) Dependence of MA on SIO thickness (*m*) in the superlattice series SL3*m*. MA is defined as the difference of remnant moment M_R between two crystallographic directions normalized by the saturation moment M_S ($(M_R[100]-M_R[110])/M_S$). The positive sign corresponds to the ⟨100⟩ easy axis whereas the negative sign indicates a $\pi/4$ shift to ⟨110⟩. The purple dot shows the anisotropy of LSMO thin film. Magnetic easy axis is shown by the arrow in the oxygen octahedral for the series of superlattices. Error bars are derived from measurements on multiple samples. (*B*) Magnetic hysteresis loops of an SL31 superlattice with magnetic field H in [100] (blue), [110] (red), and [010] (black) crystallographic orientation. (*Inset*) Plot of magnetic hysteresis loops of LSMO (20-nm) thin film on STO as a comparison. Magnetization is averaged by LSMO thickness in this study. (*C*) Schematic and polar plots of in-plane AMR. The current is along the [100] direction and the magnetic field (1 T) is rotated within the film plane. The polar plots show a phase shift of $\pi/4$ between SL33 and SL310, consistent with the thickness evolution of MA in *A*.

magnetic hysteresis loops in different orientations at multiple temperatures. Fig. 3*A* shows that the MA persists to the Curie temperature (~270 K) of the superlattice.

A close examination of the results discussed above reveals the unique nature of the MA tailoring. First, as pointed out, the MA with a π/4 phase shift of easy axis is not due to the shape anisotropy (8). Because the LSMO dominates the aggregate magnetization, one must consider the potential contribution from LSMO crystal symmetry change. Previous studies have revealed a possible mechanism that could lead to the reorientation of in-plane easy axis of LSMO thin films. It has been demonstrated that a moderate biaxial compressive strain on LSMO could lead to the orthorhombic structure and ⟨100⟩ easy axis due to the asymmetry of octahedral rotation patterns (5). RSM measurements (represented by SL35 in Fig. 1*C*) reveal that our superlattices are coherently constrained by the substrate, confirming that LSMO is under biaxial tensile strain. Another possible contribution is the interfacial octahedral coupling (31), considering the difference between LSMO and SIO (23, 26). In this scenario, one expects the rotational pattern of the LSMO to be unaltered by the thinner SIO (31); therefore, the short-period superlattice (SL31) would have a reduced tendency compared to the long-period superlattice (SL310) to show the reorientation of magnetic easy axis compared with pure LSMO film. This is however opposite to the observed thickness evolution in Fig. 2*A*. In fact, XRD measurements of several half-ordering reflections of SL31 rule out the alteration of octahedral rotation pattern as the origin (*Octahedral Rotation Pattern of Superlattices* and Fig. S3). The results thus imply a distinct role of the strong SOC in SIO to engineer the MA.

To gain more insight into the spin–orbit interaction, we investigated the valence and magnetic state of both LSMO and SIO by carrying out element selective X-ray absorption spectroscopy (XAS) and X-ray magnetic circular dichroism (XMCD) measurements (32, 33). Fig. 3 *C* and *D* shows the XAS spectra of Mn (red curve) and Ir (blue curve) of the SL31 taken at the resonant $L_{2,3}$ edges. As a comparison, XAS spectra of reference samples of LSMO (purple curve, Fig. 3*C*) and SIO (purple curve, Fig. 3*D*) thin films were taken simultaneously. The absence of peak position shift and the identical multiplet features suggest a minimal effect of charge transfer between Mn and Ir cations. Fig. 3*E* shows the Mn and Ir XMCD spectra. The large dichroism at the Mn edge is expected for the highly spin-polarized ferromagnetic LSMO and consistent with magnetometry. However, the presence of a sizable XMCD at the Ir edge reveals the onset of a net magnetization, unexpected for the paramagnetic SIO (26). To validate this observation, the XMCD spectra were taken by multiple measurements with alternated X-ray helicity and magnetic field (*Materials and Methods*). The opposite sign of dichroism of the two cations indicates that the Mn and Ir net moments are antiparallel to each other. This nontrivial coupling is further demonstrated by the coincident reversal of LSMO magnetization and Ir-XMCD (Fig. 3*B*). Furthermore, the temperature dependence of Ir-edge XMCD (Fig. 3*A*) reveals a relatively high onset temperature (near room temperature), which is closely related to the Curie temperature of LSMO. The combination of these results suggests the emergence of magnetic ordering in the nominally paramagnetic SIO in the ultrathin limit.

To understand the origins of the Ir moments, sum-rules analysis of XMCD spectra in Fig. 3*E* was applied to differentiate the spin component from the orbital counterpart (34), which yields an unexpected result. A relatively large orbital moment $\boldsymbol{m_l} = (0.036 \pm 0.003)\ \boldsymbol{\mu_b/Ir}$ is obtained for SL31 compared with the effective spin component $\boldsymbol{m_{se}} = (0.002 \pm 0.003)\ \boldsymbol{\mu_b/Ir}$ (*XMCD Characterization and Analysis* and Fig. S6). Such a large ratio of $\boldsymbol{m_l/m_{se}}$ is to date unreported even in the 5*d* TMOs. As a comparison, sum-rules analysis was also applied to the Mn L edge, which yields an $\boldsymbol{m_l/m_{se}}$ ratio less than 0.01 and is consistent with the dominant role of the spin moment for 3*d* TMOs (*XMCD Characterization and Analysis* and Fig. S7).

To further understand the magnetic behavior of SIO within the confines of the superstructure environment, we also performed first-principles density functional calculations with generalized gradient approximation (GGA) + Hubbard U + SOC (*First-Principles Calculations*). We compared the energies of configurations where the Mn moments align in the ⟨100⟩ and ⟨110⟩ directions in SL31. Because correlated oxides are notoriously challenging for GGA, we explored a variety of U parameter combinations. Whereas the magnitude of the energy difference depends on the details of the parameters, the ⟨100⟩ direction is energetically more favorable than the ⟨110⟩ direction in SL31, consistent with the experiments (Table S1). Moreover, the monolayer of SIO in SL31 develops a canted in-plane antiferromagnetic ordering (weak ferromagnetism), which is similar to the magnetic ordering of Sr_2IrO_4 (35). However, whereas the moments of Sr_2IrO_4 are known to

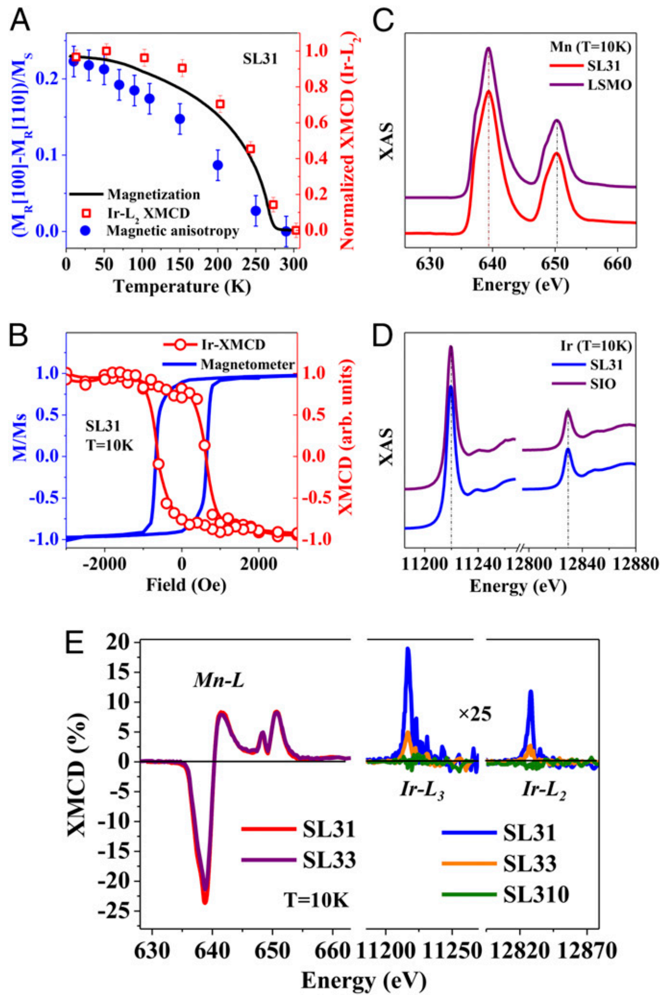

Fig. 3. XAS and XMCD spectra of the LSMO/SIO superlattice. (*A*) Temperature dependence of the magnetization, MA, and the XMCD (Ir edge) of SL31. (*B*) Field dependence of magnetization measured by magnetometer and sign of Ir-XMCD. The opposite sign corresponds to the antiparallel configuration of Mn and Ir moments in *E*. (*C* and *D*) Core-level XAS spectra of Mn and Ir of the superlattice SL31 along with the spectra of SIO and LSMO thin film (purple curve). Peak positions of the XAS spectra of the superlattice are the same as the pure thin films and the multiplet features are identical in both Ir and Mn edge within the experimental limit, suggesting the minimal effect of charge transfer in the superlattice. (*E*) XMCD spectra of the multiple superlattices measured at 10 K with 1 T applied along the [100] direction with the same photon helicity and field direction. The magnitude of XMCD is normalized by the magnitude of L_3 XAS for Mn and Ir, respectively. For comparison, the magnitude of XMCD of Ir is multiplied by a factor of 25.

align along the ⟨110⟩ direction (36, 37), the moments of SIO in SL31 prefer ⟨100⟩, highlighting a key distinction in terms of MA (Fig. S8). In summary, XMCD and first-principles calculations both reveal the emergence of the weak ferromagnetism in the ultrathin SIO, which shows an orbital-dominated moment and a different MA compared with the Ruddlesden–Popper series iridates (discussed in *Further Discussions of the MA*).

This distinctive character of the Ir moment in the superlattices presents an unconventional spin–orbit state in the iridate family. Due to the strong SOC, the low-spin d^5 configuration of Ir^{4+} valence state within the octahedral crystal field fills the *d* shell up to half of a SOC doublet ($J_{\mathrm{eff}} = 1/2$ state), which has been theoretically established (38) and experimentally observed (35) for several iridates, for example, Sr_2IrO_4. This $J_{\mathrm{eff}} = 1/2$ state, regarded as the main driver of Ir-related physics, is characterized by the distinct orbital character and orbital mixing of t_{2g} bands, leading to the ratio of $\boldsymbol{m_l/m_{se}}$ ∼0.5 (38). Experimentally it is characterized by the absence of the L_2 edge magnetic dichroism, due to dipole selection rules (35, 39). Our XMCD results of SL31 unambiguously reveal the breakdown of the $J_{\mathrm{eff}} = 1/2$ picture in the superlattices by considering how the sign and amplitude of L_2-edge and L_3-edge XMCD signatures are equivalent and comparable, respectively, thereby yielding a large $\boldsymbol{m_l/m_{se}}$ ratio as discussed above. To enhance the orbital component relative to the spin component, the new spin–orbit state is likely to be formed by mixing the $J_{\mathrm{eff}} = 1/2$ state with the $J_{\mathrm{eff}} = 3/2$ state, where the two components are antiparallel (discussed in *XMCD Characterization and Analysis*). Moreover this spin–orbit state was not reported before in the STO/SIO example (22) that is dominated by dimensional confinement, which also clearly implies the decisive role of interfacial coupling, beyond the dimensionality effects.

The emergent weak ferromagnetism in SIO exhibits a close correlation to the control of MA. As the thickness *m* reduces, the stability of ⟨100⟩ magnetic easy axis (Fig. 2*A*), the emergent weak ferromagnetism (Fig. 3*E*), and the $\boldsymbol{m_l/m_{se}}$ ratio (*XMCD Characterization and Analysis* and Fig. S6) become more significant. In addition, the emergent weak ferromagnetism shows a similar temperature dependence to that of the MA with ⟨100⟩ easy

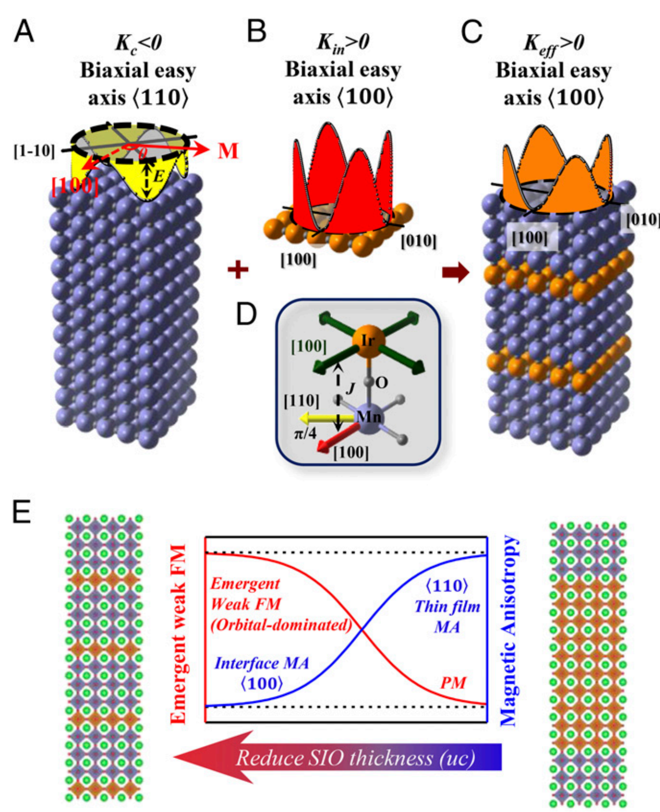

Fig. 4. Schematic diagram of the origin of the MA engineering. (*A*) MA energy of LSMO. The anisotropy energy is defined by the formula $E = K \cdot M^4 \sin^2 2\theta$, where M is the in-plane magnetization and θ is the angle to [100] (red arrows). The MCA of LSMO ($K_c <0$) favors the ⟨110⟩ easy axis as shown by the black solid lines (energy minimum). (*B*) SIO-induced MA energy ($K_{in} >0$), which favors the ⟨100⟩ easy axis. (*C*) Effective MA energy of SL31, in which the K_{in} overcomes K_c. Therefore, SL31 shows $\pi/4$ shift of the easy axis compared with LSMO. (*D*) Schematic diagram of the anisotropy contributions. The SIO-induced anisotropy is determined by the interfacial exchange coupling to the emergent weak ferromagnetism in SIO (green arrows), which effectively shifts the magnetic easy axis of LSMO by $\pi/4$. (*E*) Thickness evolution of the MA of the superlattice and the emergent magnetism in the strong SOC SIO (FM, ferromagnetic; PM, paramagnetic).

axis (Fig. 3A). Thus, the results suggest a crucial contribution to the overall MA from the interfacial magnetic coupling between the Mn spin moments and the emergent Ir orbital moments. The effective in-plane biaxial anisotropic energy is commonly defined as $E = K_{eff}M^4\sin^2 2\theta$ (40), where M is the in-plane magnetization and θ is the angle to ⟨100⟩ (Fig. 4A). Taking into account the superlattice geometry, the effective anisotropy K_{eff} is determined by the competition between MCA of LSMO (K_c) and SIO-induced anisotropy (K_{in}) (Fig. 4D). The sign of K_c remains negative due to the absence of structure change discussed before, which favors the ⟨110⟩ easy axis (Fig. 4A). The sign of K_{in} is positive, which favors the ⟨100⟩ easy axis (Fig. 4B). Therefore, in the short-period superlattices where the emergent weak ferromagnetism is more significant, K_{in} overcomes K_c and becomes dominant in K_{eff} (Fig. 4C). As m increases digitally, K_{eff} evolves from positive (K_{in}-dominated) to negative (K_c-dominated), manifesting itself as a systematic evolution of MA (Fig. 4E). The sign of K_{in} reflects the MA of the emergent Ir moment to which the Mn couples. As discussed above, in contrast to the $J_{eff} = 1/2$ RP phases Sr_2IrO_4 (35) and $Sr_3Ir_2O_7$ (41), the new spin–orbit state in the superlattices features a mixture of $J_{eff} = 1/2$ and $J_{eff} = 3/2$. Unlike $J_{eff} = 1/2$, which is actually an atomic $J = 5/2$ spin–orbit state, $J_{eff} = 3/2$ is not an eigenstate of the SOC operator, albeit being an eigenstate of the octahedral crystal-field operator. As a result, the $J_{eff} = 3/2$ wavefunctions are further hybridized with e_g orbitals and their energies acquire corrections proportional to the ratio of SOC and crystal field. Therefore, the crystal field tends to lock the total angular moment along its principal axis, e.g., ⟨100⟩, leading to a large single-ion anisotropy which is absent in $J_{eff} = 1/2$ (discussed in *Further Discussions of the MA* and Fig. S9). Thus, the mixture of $J_{eff} = 1/2$ and $J_{eff} = 3/2$, which can be engineered in the superlattices, controls the MA of the emergent Ir moment. This result proffers a new control paradigm in correlated electron behavior.

In conclusion, we present the ability to engineer the MA of ferromagnetic LSMO by inserting the strong SOC paramagnet SIO with atomically controlled thickness. The origin is attributed to a novel SOC state with a relatively large orbital-dominated moment that develops in the typically paramagnetic SIO. Our results demonstrate the potential of combined artificial confinement and interfacial coupling to discover new phases as well as to control the functionalities. This study particularly expands the current research interest of the atomic-scale engineering toward the strong SOC *5d* TMOs, which also paves the way toward all-oxide spintronics.

Materials and Methods

Synthesis. $(LSMO)_3(SIO)_m$ superlattices with different m were grown by RHEED-assisted pulsed laser disposition on low-miscut STO substrates. Before the growth, the substrates were wet-etched by buffered HF acid, followed by a thermal annealing process at 1,000 °C for 3 h in oxygen atmosphere. Both LSMO and SIO sublayers were deposited at 700 °C and 150-mtorr oxygen partial pressure from the chemical stoichiometric ceramic target by using the KrF excimer laser (248 nm) at the energy density of 1.5 J/cm^2. The repetition rate was 1 Hz and 10 Hz for each sublayer. During the growth, in situ RHEED intensity oscillations were monitored to control the growth at the atomic scale. After growth the samples cooled down at the rate of 5 °C/min in pure oxygen atmosphere.

Magnetic and Transport Measurement. Magnetic measurements were performed on the Quantum Design Superconducting Quantum Interference Device (SQUID) magnetometry with an Reciprocating Sample Option (RSO) option, which provides a sensitivity of 10^{-7} emu. To study the MA, magnetization loops were measured along different crystallographic directions of SL3*m*: in-plane [100], in-plane [110], and out-of-plane [001]. Also, magnetization loops were measured along symmetry-equivalent in-plane directions, e.g., [100] and [010], to check the angle dependence of MA. Transport measurements were performed using the Quantum Design Physical Property Measurement System (PPMS, 14T). The longitudinal resistance is measured by the four-point probes method with the excitation current (10 μA) flowing in the film plane (crystallographic [100], shown in Fig. 2C). The relative angle between the magnetic field and current was controlled by rotating the sample holder. The magnetic hysteresis loops and AMR curves reported here have been reproduced on multiple samples.

XAS, XMCD, and XRD Measurement. The XAS and XMCD characterizations at the Mn edge were carried out at beamline 4.0.2 at the Advanced Light Source, Lawrence Berkeley National Laboratory. The measurements were performed using the total-electron-yield mode and the angle of incident beam is 30° to the sample surface. The XAS and XMCD characterizations at the Ir edge were carried at beamline 4-ID-D at Advanced Photon Source (APS) in Argonne National Laboratory. The results were taken by collecting the fluorescence yield signal and the incident beam is 3° to the sample surface. All of the XMCD spectra were measured both in remanence and in saturation field. Experimental artifacts were ruled out by changing both the photon helicity and the magnetic field direction. Because the XMCD spectra of the Ir edge are relatively weak, multiple measurements were repeated to increase the signal-to-noise ratio of the spectra (five times for each spectrum at each field). Also we measured the spectra at different times and on different samples. The hysteresis loop of the Ir-XMCD was measured with energy fixed at 12.828 keV (maximum of L_2 XMCD) by altering the photon helicity at each magnetic field. Synchrotron XRD measurements were carried out at sector 33BM and 6-ID-B at APS in Argonne National Laboratory.

ACKNOWLEDGMENTS. We acknowledge Dr. D. Haskel, S. Cheema, E. A. Karapetrova, and Dr. J. H. Chu for experiment assistance and Professor L. W. Martin, Professor M. van Veenendaal, and Professor E. Dagotto for critical discussions. This work was funded by the Director, Office of Science, Office of Basic Energy Sciences, Materials Science and Engineering Department of the US Department of Energy (DOE) in the Quantum Materials Program (KC2202) under Contract No. DE-AC02-05CH11231. D.Y. is supported by the National Science Foundation through Materials Research Science and Engineering Centers Grant DMR 1420620. We acknowledge additional support for the research at University of California, Berkeley through the US Department of Defense (DOD) Army Research Office (ARO) Multidisciplinary University Research Initiatives (MURI) Program, Defense Advanced Research Projects Agency (DARPA) and Center for Energy Efficient Electronics Science (E3S). Research at the University of Tennessee (J.L., L.Z., and H.X.) is sponsored by the Science Alliance Joint Directed Research and Development Program. This research used resources of The National Institute for Computational Sciences at the University of Tennessee under Contract UT-TENN0112. This research used resources of the Advanced Photon Source, a US DOE Office of Science User Facility operated for the DOE Office of Science by Argonne National Laboratory under Contract DE-AC02-06CH11357. Use of the Advanced Light Source is supported by the Director, Office of Science, Office of Basic Energy Sciences, of the US DOE under Contract DE-AC02-05CH11231. Work at the National Center for Electron Microscopy, Molecular Foundry is supported by the Office of Science, Office of Basic Energy Sciences, of the US DOE under Contract DE-AC02-05CH11231.

1. Otte AF, et al. (2008) The role of magnetic anisotropy in the Kondo effect. *Nat Phys* 4(11):847–850.
2. Reis MS, et al. (2008) Influence of the strong magnetocrystalline anisotropy on the magnetocaloric properties of MnP single crystal. *Phys Rev B* 77(10):8.
3. Rössler UK, Bogdanov AN, Pfleiderer C (2006) Spontaneous skyrmion ground states in magnetic metals. *Nature* 442(7104):797–801.
4. Matsukura F, Tokura Y, Ohno H (2015) Control of magnetism by electric fields. *Nat Nanotechnol* 10(3):209–220.
5. Boschker H, et al. (2011) Uniaxial contribution to the magnetic anisotropy of $La_{0.67}Sr_{0.33}MnO_3$ thin films induced by orthorhombic crystal structure. *J Magn Magn Mater* 323(21):2632–2638.
6. Valencia S, Balcells L, Martinez B, Fontcuberta J (2003) Thickness dependence of the magnetic anisotropy in $La_{2/3}Ca_{1/3}MnO_3$ thin films grown on $LaAlO_3$ substrates. *J Appl Phys* 93(10):8059–8061.
7. Tsui F, Smoak MC, Nath TK, Eom CB (2000) Strain-dependent magnetic phase diagram of epitaxial $La_{0.67}Sr_{0.33}MnO_3$ thin films. *Appl Phys Lett* 76(17):2421–2423.
8. Mathews M, et al. (2005) Step-induced uniaxial magnetic anisotropy of $La_{0.67}Sr_{0.33}MnO_3$ thin films. *Appl Phys Lett* 87(24):3.
9. Nogues J, Schuller IK (1999) Exchange bias. *J Magn Magn Mater* 192(2):203–232.
10. Pesin D, Balents L (2010) Mott physics and band topology in materials with strong spin-orbit interaction. *Nat Phys* 6(5):376–381.
11. Wang F, Senthil T (2011) Twisted Hubbard model for Sr_2IrO_4: Magnetism and possible high temperature superconductivity. *Phys Rev Lett* 106(13):136402.
12. Xiao D, Zhu W, Ran Y, Nagaosa N, Okamoto S (2011) Interface engineering of quantum Hall effects in digital transition metal oxide heterostructures. *Nat Commun* 2:596.
13. Seki T, et al. (2008) Giant spin Hall effect in perpendicularly spin-polarized FePt/Au devices. *Nat Mater* 7(2):125–129.

APPLIED PHYSICAL SCIENCES

14. Saitoh E, Ueda M, Miyajima H, Tatara G (2006) Conversion of spin current into charge current at room temperature: Inverse spin-Hall effect. *Appl Phys Lett* 88(18): 182509.
15. Johnson MT, Bloemen PJH, denBroeder FJA, deVries JJ (1996) Magnetic anisotropy in metallic multilayers. *Rep Prog Phys* 59(11):1409–1458.
16. Ravindran P, et al. (2001) Large magnetocrystalline anisotropy in bilayer transition metal phases from first-principles full-potential calculations. *Phys Rev B* 63(14): 144409.
17. Boris AV, et al. (2011) Dimensionality control of electronic phase transitions in nickel-oxide superlattices. *Science* 332(6032):937–940.
18. Gibert M, Zubko P, Scherwitzl R, Iñiguez J, Triscone J-M (2012) Exchange bias in $LaNiO_3$-$LaMnO_3$ superlattices. *Nat Mater* 11(3):195–198.
19. King PDC, et al. (2014) Atomic-scale control of competing electronic phases in ultrathin $LaNiO_3$. *Nat Nanotechnol* 9(6):443–447.
20. Monkman EJ, et al. (2012) Quantum many-body interactions in digital oxide superlattices. *Nat Mater* 11(10):855–859.
21. Hwang HY, et al. (2012) Emergent phenomena at oxide interfaces. *Nat Mater* 11(2): 103–113.
22. Matsuno J, et al. (2015) Engineering a spin-orbital magnetic insulator by tailoring superlattices. *Phys Rev Lett* 114(24):247209.
23. Tokura Y (2006) Critical features of colossal magnetoresistive manganites. *Rep Prog Phys* 69(3):797–851.
24. Berndt LM, Balbarin V, Suzuki Y (2000) Magnetic anisotropy and strain states of (001) and (110) colossal magnetoresistance thin films. *Appl Phys Lett* 77(18):2903–2905.
25. Moon SJ, et al. (2008) Dimensionality-controlled insulator-metal transition and correlated metallic state in 5d transition metal oxides $Sr_{n+1}Ir_nO_{3n+1}$ (n=1, 2, and infinity). *Phys Rev Lett* 101(22):226402.
26. Zhao JG, et al. (2008) High-pressure synthesis of orthorhombic $SrIrO_3$ perovskite and its positive magnetoresistance. *J Appl Phys* 103(10):5.
27. Nie YF, et al. (2015) Interplay of spin-orbit interactions, dimensionality, and octahedral rotations in semimetallic $SrIrO_3$. *Phys Rev Lett* 114(1):016401.
28. Chen Y, Lu Y-M, Kee H-Y (2015) Topological crystalline metal in orthorhombic perovskite iridates. *Nat Commun* 6:6593.
29. Liu J, et al. (2016) Strain-induced nonsymmorphic symmetry breaking and removal of Dirac semimetallic nodal line in an orthoperovskite iridate. *Phys Rev B* 93(8):085118.
30. Carter J-M, Shankar VV, Zeb MA, Kee H-Y (2012) Semimetal and topological insulator in perovskite iridates. *Phys Rev B* 85(11):115105.
31. Rondinelli JM, May SJ, Freeland JW (2012) Control of octahedral connectivity in perovskite oxide heterostructures: An emerging route to multifunctional materials discovery. *MRS Bull* 37(3):261–270.
32. Abbate M, et al.; de Groot FM (1992) Controlled-valence properties of $La_{1-x}Sr_xFeO_3$ and $La_{1-x}Sr_xMnO_3$ studied by soft-x-ray absorption spectroscopy. *Phys Rev B Condens Matter* 46(8):4511–4519.
33. Mugavero SJ, 3rd, Smith MD, Yoon WS, zur Loye HC (2009) $Nd_2K_2IrO_7$ and $Sm_2K_2IrO_7$: Iridium(VI) oxides prepared under ambient pressure. *Angew Chem Int Ed Engl* 48(1): 215–218.
34. Stöhr J (1999) Exploring the microscopic origin of magnetic anisotropies with X-ray magnetic circular dichroism (XMCD) spectroscopy. *J Magn Magn Mater* 200(1–3): 470–497.
35. Kim BJ, et al. (2009) Phase-sensitive observation of a spin-orbital Mott state in Sr_2IrO_4. *Science* 323(5919):1329–1332.
36. Boseggia S, et al. (2013) Robustness of basal-plane antiferromagnetic order and the $J_{(eff)}$=1/2 state in single-layer iridate spin-orbit Mott insulators. *Phys Rev Lett* 110(11):117207.
37. Katukuri VM, et al. (2014) Mechanism of basal-plane antiferromagnetism in the spin-orbit driven iridate Ba_2IrO_4. *Phys Rev X* 4(2):021051.
38. Kim BJ, et al. (2008) Novel Jeff=1/2 Mott state induced by relativistic spin-orbit coupling in Sr2IrO4. *Phys Rev Lett* 101(7):076402.
39. Haskel D, et al. (2012) Pressure tuning of the spin-orbit coupled ground state in Sr_2IrO_4. *Phys Rev Lett* 109(2):027204.
40. Ziese M, Semmelhack HC, Busch P (2002) Sign reversal of the magnetic anisotropy in La0.7A0.3MnO3 (A=Ca, Sr, Ba) films. *J Magn Magn Mater* 246(1–2):327–334.
41. Kim JW, et al. (2012) Dimensionality driven spin-flop transition in layered iridates. *Phys Rev Lett* 109(3):037204.
42. Glazer AM (1975) Simple ways of determining perovskite structures. *Acta Crystallogr, Sect A* 31(NOV1):756–762.
43. Zhai X, et al. (2014) Correlating interfacial octahedral rotations with magnetism in $(LaMnO_{3+\delta})_N/(SrTiO_3)_N$ superlattices. *Nat Commun* 5:4283.
44. Izumi M, et al. (2001) Insulator-metal transition induced by interlayer coupling in $La_{0.6}Sr_{0.4}$MnO3/$SrTiO_3$ superlattices. *Phys Rev B* 64(6):064429.
45. Bruno FY, et al. (2011) Electronic and magnetic reconstructions in $La_{0.7}Sr_{0.3}$MnO3/$SrTiO_3$ heterostructures: A case of enhanced interlayer coupling controlled by the interface. *Phys Rev Lett* 106(14):147205.
46. Bibes M, et al. (2000) Anisotropic magnetoresistance of (0 0 h), (0 h h) and (h h h) $La_{2/3}Sr_{1/3}MnO_3$ thin films on (0 0 1) Si substrates. *J Magn Magn Mater* 211(1–3):206–211.
47. Chen CT, et al. (1995) Experimental confirmation of the X-ray magnetic circular dichroism sum rules for iron and cobalt. *Phys Rev Lett* 75(1):152–155.
48. Teramura Y, Tanaka A, Jo T (1996) Effect of Coulomb interaction on the X-ray magnetic circular dichroism spin sum rule in 3 d transition elements. *J Phys Soc Jpn* 65(4):1053–1055.
49. Kresse G, Hafner J (1993) *Ab initio* molecular dynamics for liquid metals. *Phys Rev B Condens Matter* 47(1):558–561.
50. Kresse G, Furthmüller J (1996) Efficient iterative schemes for *ab initio* total-energy calculations using a plane-wave basis set. *Phys Rev B Condens Matter* 54(16): 11169–11186.
51. Liechtenstein AI, Anisimov VI, Zaanen J (1995) Density-functional theory and strong interactions: Orbital ordering in Mott-Hubbard insulators. *Phys Rev B Condens Matter* 52(8):R5467–R5470.
52. Kim KH, Kim HS, Han MJ (2014) Electronic structure and magnetic properties of iridate superlattice $SrIrO_3/SrTiO_3$. *J Phys: Condens Matter* 26(18):5.
53. Rabe KM (2010) First-principles calculations of complex metal-oxide materials. *Annu Rev Condens Matter Phys* 1(1):211–235.
54. Jeng H-T, Guo GY (2002) First-principles investigations of the electronic structure and magnetocrystalline anisotropy in strained magnetite Fe_3O_4. *Phys Rev B* 65(9):094429.
55. Moretti Sala M, et al. (2014) Crystal field splitting in $Sr_{n+1}Ir_nO_{3n+1}$ (n=1, 2) iridates probed by x-ray Raman spectroscopy. *Phys Rev B* 90(8):085126.